



Titre: Terahertz dielectric spectroscopy and solid immersion microscopy of
Title: ex vivo glioma model 1018: brain tissue heterogeneity

Auteurs: A. S. Kucheryavenko, N. V. Chernomyrdin, A. A. Gavidush, A. I.
Alekseeva, P. V. Nikitin, I. N. Dolganova, P. A. Karalkin, A. S.
Authors: Khalansky, I. E. Spektor, Maksim A. Skorobogatiy, V. V. Tuchin, & K. I.
Zaytsev

Date: 2021

Type: Article de revue / Article

Référence: Kucheryavenko, A. S., Chernomyrdin, N. V., Gavidush, A. A., Alekseeva, A. I.,
Nikitin, P. V., Dolganova, I. N., Karalkin, P. A., Khalansky, A. S., Spektor, I. E.,
Skorobogatiy, M. A., Tuchin, V. V., & Zaytsev, K. I. (2021). Terahertz dielectric
Citation: spectroscopy and solid immersion microscopy of ex vivo glioma model 1018:
brain tissue heterogeneity. Biomedical Optics Express, 12(8), 5272-5289.
<https://doi.org/10.1364/boe.432758>

 **Document en libre accès dans PolyPublie**
Open Access document in PolyPublie

URL de PolyPublie: <https://publications.polymtl.ca/9355/>
PolyPublie URL:

Version: Version officielle de l'éditeur / Published version
Révisé par les pairs / Refereed

Conditions d'utilisation: OSA Open Access Publishing Agreement
Terms of Use:

 **Document publié chez l'éditeur officiel**
Document issued by the official publisher

Titre de la revue: Biomedical Optics Express (vol. 12, no. 8)
Journal Title:





Maison d'édition: Optica Publishing Group
Publisher:

URL officiel: <https://doi.org/10.1364/boe.432758>
Official URL:

Mention légale: © 2021 Optical Society of America under the terms of the OSA Open Access Publishing
Legal notice: Agreement



Terahertz dielectric spectroscopy and solid immersion microscopy of *ex vivo* glioma model 101.8: brain tissue heterogeneity

A. S. KUCHERYAVENKO,^{1,2} N. V. CHERNOMYRDIN,^{1,3,12} A. A. GAVDUSH,^{1,3} A. I. ALEKSEEVA,⁴ P. V. NIKITIN,^{1,5,6} I. N. DOLGANOVA,^{2,3,5}  P. A. KARALKIN,⁷ A. S. KHALANSKY,⁴ I. E. SPEKTOR,¹ M. SKOROBOGATYI,⁸  V. V. TUCHIN,^{9,10,11}  AND K. I. ZAYTSEV^{1,3,13} 

¹Prokhorov General Physics Institute of the Russian Academy of Sciences, Russia

²Institute of Solid State Physics of the Russian Academy of Sciences, Russia

³Bauman Moscow State Technical University, Russia

⁴Research Institute of Human Morphology, Russia

⁵Institute for Regenerative Medicine, Sechenov University, Russia

⁶Burdenko Neurosurgery Institute, Russia

⁷Institute for Cluster Oncology, Sechenov University, Russia

⁸Department of Engineering Physics, Polytechnique Montreal, Canada

⁹Science Medical Center, Saratov State University, Russia

¹⁰Institute of Precision Mechanics and Control of the Russian Academy of Sciences, Russia

¹¹National Research Tomsk State University, Russia

¹²chernik-a@yandex.ru

¹³kirzay@gmail.com

Abstract: Terahertz (THz) technology holds strong potential for the intraoperative label-free diagnosis of brain gliomas, aimed at ensuring their gross-total resection. Nevertheless, it is still far from clinical applications due to the limited knowledge about the THz-wave–brain tissue interactions. In this work, rat glioma model 101.8 was studied *ex vivo* using both the THz pulsed spectroscopy and the 0.15 λ -resolution THz solid immersion microscopy (λ is a free-space wavelength). The considered homograft model mimics glioblastoma, possesses heterogeneous character, unclear margins, and microvasculature. Using the THz spectroscopy, effective THz optical properties of brain tissues were studied, as averaged within the diffraction-limited beam spot. Thus measured THz optical properties revealed a persistent difference between intact tissues and a tumor, along with fluctuations of the tissue response over the rat brain. The observed THz microscopic images showed heterogeneous character of brain tissues at the scale posed by the THz wavelengths, which is due to the distinct response of white and gray matters, the presence of different neurovascular structures, as well as due to the necrotic debris and hemorrhage in a tumor. Such heterogeneities might significantly complicate delineation of tumor margins during the intraoperative THz neurodiagnosis. The presented results for the first time pose the problem of studying the inhomogeneity of brain tissues that causes scattering of THz waves, as well as the urgent need to use the radiation transfer theory for describing the THz-wave — tissue interactions.

© 2021 Optical Society of America under the terms of the [OSA Open Access Publishing Agreement](#)

1. Introduction

Terahertz (THz) technology went through rapid development during the past few decades [1]. Nowadays, it offers novel opportunities in the label-free diagnosis of malignant and benign neoplasms with different nosologies and localizations [2–5]. Such applications rely on strong sensitivity of THz waves to the content and state of tissue water, which serves as the main

endogenous label of pathological processes in tissues [6]. Despite a shallow depth of THz-wave penetration into tissues ($\sim 10^{-1}$ – 10^{-2} mm), which is due to strong THz-wave absorption by tissue water, THz instruments can be applied to probe superficial tissues either non-invasively or intraoperatively. Among the novel exciting applications of THz technology, we mention the intraoperative diagnosis of human brain gliomas of the different World Health Organization (WHO) grades [7], where THz spectroscopy and imaging might help with the intraoperative delineation of tumor margins, aimed at ensuring its gross-total resection and, thus, improving the patient's survival and quality of life [8].

Gliomas are among the most common and deadly pathologies of the brain, that constitute $\approx 26\%$ of all primary tumors and $\approx 81\%$ of primary malignant tumors of the brain [9]. They are classified into the WHO Grades I to IV, where Grades I, II are the low-grade gliomas, while Grades III, IV – the high-grade ones [7]. Among all gliomas, glioblastoma (WHO Grade IV glioma) remains the most dangerous one, with the five-year relative survival rate of only $\approx 6.8\%$ [9]. Surgery remains the mainstay of the treatment for all grades of glial tumors, while their gross-total resection with maximal preservation of intact brain forms a main goal of surgical treatments [10]. In many cases, even when the desired gross-total resection is achieved, the tumor can relapse due to its infiltrative and disseminated growth nature, since single tumor cells can be found at a considerable distance from the tumor [11]. Gliomas usually possess unclear margins, which complicates their gross-total resection. Accurate delineation of glioma margins is a daunting task and can be provided only by the *ex vivo* histopathological examination of the excised tissues, using the Hematoxylin and Eosin (H&E)-stained histology aided by the molecular sensing and genetics [12]. Such studies of brain tissues can be performed either intraoperatively (thus, extending the terms of surgery) or postoperatively (thus, confirming the gross total resection of a tumor). Despite the fact that histopathology still remains a gold standard in diagnosis of the central nervous system tumors, increasing demand for the development of novel methods for rapid intraoperative detection of the tumor margins is evident, thus, pushing further research into discovering novel modalities of brain tissues imaging and spectroscopy.

Common methods of pre-operative imaging, such as Magnetic Resonance Imaging (MRI), computer and positron emission tomography, do not provide reliable accuracy of the tumor margins detection due to possible brain shifts, caused by the dura mater opening, tumor removal, brain tissue edema, and cerebrospinal fluid losses [13]. As a compromise, real-time imaging techniques, such as the intraoperative ultrasound and MRI, along with algorithms that reconcile preoperative MRI and intraoperative ultrasound imaging data were developed [14]. However, these instruments suffer from low spatial resolution, while their integration into modern neurosurgical workflows remains labor intensive and expensive. Another group of widespread intraoperative neuroimaging methods includes fluorescent-based techniques involving the use of the 5-aminolevulinic acid-induced fluorescence of protoporphyrin IX [15], fluorescein sodium [16], or other mostly exogenous fluorophores. They are inexpensive and demonstrate high sensitivity in surgery of high-grade gliomas and meningiomas; while their sensitivity decreases for the pediatric tumors and low-grade gliomas [17]. Other optical modalities of the intraoperative brain tissue imaging, such as optical coherence tomography [18,19], Raman spectroscopy and imaging [20], confocal and polarization-sensitive microscopy [21,22], visible and near infrared spectroscopy [23], and photoacoustic imaging [24], are vigorously explored, but they are still far from clinics. Their efficiency is limited by a number of factors, including the brain shift, application of contrast agents, limited sensitivity and specificity, and high labor intensity. Obviously, all these factors postpone the clinical implementation of these methods.

Recently, THz spectroscopy and imaging were studied as innovative tools for the intraoperative neurodiagnosis [8]. In Ref. [25], orthotopic glioma model from rats was imaged *ex vivo* in the THz range. The observed results revealed differences between intact tissues and glioma model in both freshly-excised and paraffin-embedded (dehydrated) tissues. For the freshly-excised tissues, they

were attributed to the increased water content in a tumor due to the abnormal microvascularization, edema, and body fluids around necrotic debris. In turn, for the paraffin-embedded tissues, they were less pronounced and reportedly originate from changes in cell density in a tumor. In Ref. [26], paraffin-embedded intact tissues and glioma model (GL261 cell line) from mice were studied *ex vivo* using THz pulsed spectroscopy, while the observed data justified a contrast between intact tissues and a tumor in the THz range. In Ref. [27], intact tissues and glioma model (C6 cell line) from rats were studied. As a result of THz measurements, an increased water content in a tumor was demonstrated and reported as the main reason of contrast between intact tissues and a tumor. In Refs. [28–30], a potential of THz reflectometry and imaging for brain tumor diagnosis was highlighted few more times involving *ex vivo* and *in vivo* glioma models from mice and rats (eGFP+GSC-11, C6, and U87-MG cell lines), and few samples of human high-grade gliomas *ex vivo*.

Since glioma models only partially mimic biophysical properties of human brain tumors, in our previous work, THz pulsed spectroscopy was applied to study *ex vivo* optical properties of gelatin-embedded intact tissues and WHO Grades I–IV gliomas of the human brain [31]. Gelatin slabs were used to preserve tissues from hydration/dehydration during the THz measurements and, thus, to sustain their THz response unaltered as compared to the freshly-excised tissues [32]. Statistical differences between the THz optical properties of intact tissues and gliomas of all WHO grades were revealed, while the response of edematous tissue was very close to that of a tumor. Edema, along with traumatic brain injuries [33,34], contains increased amount of tissue water and, thus, can be confused with a tumor. Next, in Ref. [35], we developed physical models, which describe the effective THz complex dielectric permittivity of intact tissues, edema, and WHO Grade I–IV gliomas of the human brain. Such models assume the tissues to be homogeneous at the scale posed by the THz wavelengths and describe completely the interactions between THz waves and tissues in the framework of classical electrodynamics and the effective medium theory. Thus developed models confirmed increased water content in the edematous tissues and WHO Grade I–IV gliomas.

Despite a considerable progress, THz technology still remains far from the clinical neurodiagnosis, primarily, due to the limited knowledge about the THz-wave – brain tissue interactions. In majority of the aforementioned studies, considerable variation in the measured effective THz optical properties of brain tissues (averaged within the diffraction-limited THz beam spot) was observed; for example, see Refs. [31,35]. Such variability was attributed to the natural fluctuations of the effective THz response of the brain tissues, as well as to the mesoscale heterogeneities of the brain. Such brain tissue heterogeneity cannot be described in the framework of the effective medium theory. On the one hand, it can complicate the THz diagnosis of brain tumors; on the other hand, it can even become a source of additional useful information for the intraoperative tissue differentiation. Obviously, this deserves further comprehensive studies.

To address this challenge, in this work, we study glioma model 101.8 from rats *ex vivo* using both the diffraction-limited THz pulsed spectroscopy and the innovative THz solid immersion microscopy, which overcomes the Abbe diffraction limit and provides the advanced spatial resolution of up to 0.15λ (λ is a free-space wavelength). This particular homograft glioma model mimics glioblastoma (i.e., the WHO Grade IV glioma of the human brain), while featuring heterogeneous character, unclear margins, and microvasculature. Our THz measurements yield the effective THz optical properties of the freshly-excised intact tissues and a tumor *ex vivo*. THz spectroscopic data show a moderate label-free contrast between these tissues in the THz range, as well as a considerable natural variability of the tissue response over the rat brain. Next, the THz solid immersion microscopy is used to obtain images of the intact rat brain and a tumor with essentially sub-wavelength spatial resolution. By comparing THz microscopy of the freshly-excised and paraffin-embedded (dehydrated) tissues, we confirm that tissue water serves as the main endogenous label of brain tumors in the THz range. Finally, THz microscopy

uncovers the origin of brain tissue heterogeneity at a scale posed at the THz-wavelength scale. Thus, heterogeneous character of the intact brain is primarily due to distinct THz response of white and gray matters, and due to other neurovascular structures, while that of a tumor is caused by the necrotic debris and hemorrhage. Thus, by studying brain tissues with such a high spatial resolution, their heterogeneous character at the THz-wavelength scale was experimentally uncovered for the first time. The observed heterogeneities of intact rat brain and a tumor might make the intraoperative THz delineation of tumor margins quite a daunting or even impossible task. Our findings pose important problems of studying the tissue heterogeneity and the related THz-wave scattering effects in different branches of THz biophotonics. In our opinion, the radiation transfer theory can pave the way for proper description of the interactions between the THz waves and tissues, and further studies in this direction are in order.

2. Materials and methods

2.1. Homograft glioma model 101.8 from rats

In all previous THz measurements of animal brain tumors [25–30], only the xenograft models were considered. Such models imply xenotransplantation of human tumor cell lines into animal brain, which results in growth of a tumor with quite clear margins, that can be detected even with the naked eye and that can be surrounded by a layer of free water. Such xenograft models fail to mimic microvasculature and diffuse margins of a tumor and, thus, seem to be sub-optimal for examining the performance of novel intraoperative imaging modalities.

In turn, a homograft glioma model 101.8 [36] involves injection of rat brain glioma tissues into the brain of another rat. This model was obtained and is kept in the collection of the Research Institute of Human Morphology (Moscow, Russia), being compliant with glioblastoma (WHO Grade IV glioma) [7] and applied in different branches of experimental neurooncology. Glioma 101.8 mimics unclear (diffuse) margins and tissue heterogeneities, including necrosis, hemorrhage, and even microvasculature, that are usually inherent to gliomas of the human brain. In this way, such model is perfectly suitable for evaluating the performance of novel modalities of brain tissue imaging [18].

In this work, we studied glioma model 101.8 using the THz pulsed spectroscopy, THz solid immersion microscopy, and Hematoxylin and Eosin (H&E)-stained histology, aimed at uncovering advantages and drawbacks of THz spectroscopy and imaging in the intraoperative neurodiagnosis. The work with animals was carried out in accordance with the ethical principles established by the European Convention for the Protection of Vertebrate Animals used for Experimental and Other Scientific Purposes (Strasbourg, 2006) and the International Guidelines for Biomedical Research in Animals (CIOMS and ICLAS, 2012).

Tumor transplantation into the brain of Wistar rats was performed as described in Ref. [37]. Approximately 14–18 days after the transplantation, animals with clinical signs of intracerebral tumor growth (increasing paresis, hyperkinesia, and, at the final stage, bloody effusion on the eyelids and nose) were sacrificed by carbon dioxide asphyxiation. Then, the cranium was opened and the whole rat brain was removed. The location of the tumor was easily identified visually. A scalpel incision was made in the frontal plane approximately through the center of the neoplasm. The dissected brain fragment was placed on the object windows of the THz pulsed spectrometer or the THz solid immersion microscope, as it is discussed below. Thus, the front (incision) side of the brain was in contact with the object window, while its back side was covered by the polyethylene film during THz measurements, in order to prevent the tissue from hydration/dehydration.

After THz measurements, tissue specimens were fixed in a 4% paraformaldehyde solution for 48 hours and, then, embedded into paraffin blocks. A routine H&E-staining of 5- μ m-thick tissues section was performed. First, 5 sections were used for the examining and mapping the area of interest. Then, they underwent a histological examination with marking of white and

gray matter, tumor margins, areas of infiltrative germination, as well as foci of necrosis, vessels and hemorrhages. These histological data served as a reference and validation tool for our THz measurements. Finally, residual dehydrated tissues in paraffin blocks were additionally studied by the THz microscopy, and the observed results were compared with the THz measurements of freshly-excised tissues and the H&E-stained histology data.

2.2. THz pulsed spectroscopy

First, freshly-excised intact tissues and glioma model 101.8 from rats were measured using a portable THz pulsed spectrometer zOmega MicroZ, that was used and detailed in our previous studies [38,39]. It was adapted for the reflection-mode measurements, as shown in Fig. 1, while a tissue specimen was handled at the shadow side of a crystalline quartz window. The High-Density PolyEthylene (HDPE) lens, with the focal length of $f \approx 75$ mm and the diameter of $D \approx 25$ mm, was used to focus the THz beam into diffraction-limited spot of radius

$$r = 1.22 \frac{f}{D n_{\text{SiO}_2} \lambda} \approx 1.7 \lambda, \quad (1)$$

where $n_{\text{SiO}_2} \approx 2.15$ is the ordinary refractive index of the crystalline quartz at THz frequencies [31]. Tissues are aligned with respect to the THz-beam spot with the help of a visible laser pointer and a digital camera. Due to the selected measurement geometry, finite dynamic range of our system, and fluctuations of humidity along the THz beam path (no vacuum pump or nitrogen gas purging are used), the spectral range of tissue characterization is limited by 0.2–1.1 THz, while the spectral resolution is ≈ 50 GHz. Despite such a limited performance of this commercial THz pulsed spectrometer, it appears to be quite convenient for a rapid tissue characterization; therefore, in this study, we resorted to this portable system from the earlier-reported labour in-house ones (for example, see Refs. [31,35]), aimed at confirming the contrast between intact tissues and tumors of the brain.

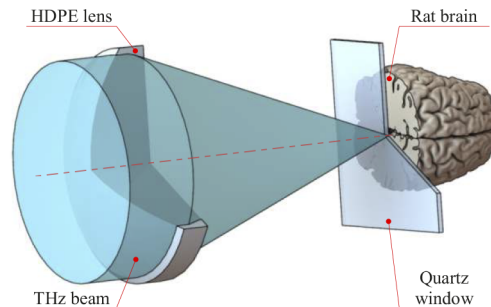


Fig. 1. Schematic of the rat brain imaging *ex vivo* using the THz pulsed spectrometer.

For the THz optical properties estimation, two THz waveforms were detected: a sample one E_s – with a tissue specimen behind the quartz window, and a reference one E_r – with a free space in place of a sample. In Figs. 2(a),(b), examples of the two waveforms and their Fourier spectra are shown. Both waveforms are comprised of three distinct wavelets, denoted as I, II and III in Fig. 2(a). Wavelet I is equal for the reference and sample waveforms, since it reflects from the “free space–quartz” interface. Wavelet II holds information about the THz-wave reflected from the “quartz–free space” or “quartz–tissue” interfaces for the reference and sample waveforms, respectively. Finally, wavelet III is due to the THz standing wave resonance inside a quartz window. Interference of these three wavelets causes a pronounced oscillation in the frequency domain; see Fig. 2(b),

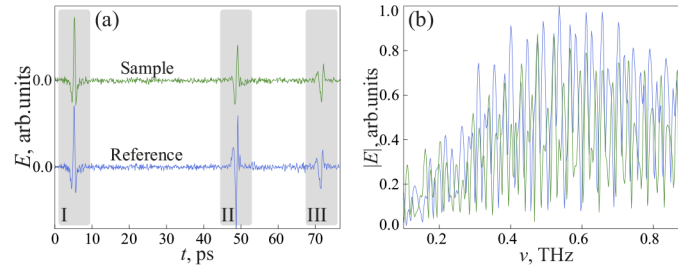


Fig. 2. THz pulsed spectroscopy of intact rat brain and glioma model 101.8 *ex vivo*: (a) Examples of the reference and sample (intact rat brain) THz waveforms. (b) Their Fourier spectra. In (a), gray-colored areas and markers I and II denote the THz wavelets, that are reflected from the "free-space – quartz" and "quartz – tissue" (or "quartz – free space") interfaces, respectively; while marker III stands for the wavelet caused by the longitudinal THz-wave resonance inside a quartz window.

By processing these waveforms (with an emphasis on wavelets II), we can reconstruct the effective complex refractive index of brain tissues

$$\tilde{n} = n - i \frac{c_0}{2\pi\nu} \alpha, \quad (2)$$

where n is a refractive index, α is an absorption coefficient (by field) in $[\text{cm}^{-1}]$, ν is a frequency, and $c_0 = 3 \times 10^8$ m/sec is the speed of light in free space. For reconstruction of the tissue optical properties based on the reference E_r and sample E_s waveforms, a procedure from Ref. [31] was applied. It is based on a plane wave approximation, that is typical for THz spectroscopic measurements with a low-aperture optical system [31,38,39]. It implies apodization (i.e., time-domain window filtering) of each waveform by a 20-ps-width 4th-order Blackman-Harris window, that is centered at the maximum of a THz wavelet II in a waveform (see Fig. 2(a)), thus, filtering out contributions of the wavelets I, III. Evidently, the wavelet II features information about the THz-wave reflection from the "quartz–tissue" or "quartz–free space" interfaces for the sample and reference waveforms, respectively.

Then, complex refractive index of tissues is determined via minimization of the vector error functional, which is defined in the Fourier domain based on theoretical H_{th} and experimental H_{exp} transfer functions:

$$\tilde{n} = \text{argmin}_{\tilde{n}} [\Phi], \quad \Phi = \left(\begin{array}{c} |H_{\text{th}}| - |H_{\text{exp}}| \\ \varphi |H_{\text{th}}| - \varphi |H_{\text{exp}}| \end{array} \right), \quad (3)$$

where $|\dots|$ and $\varphi[\dots]$ define modulus and phase operators, respectively. The function H_{exp} is computed using the frequency-domain sample E_s and reference E_r signals after the apodization

$$H_{\text{exp}} = \frac{E_s}{E_r}. \quad (4)$$

The function H_{th} is computed using the Fresnel formulas for the electromagnetic field reflection

$$H_{\text{th}} = \frac{r_{\text{quartz-tissue}}}{r_{\text{quartz-air}}}, \quad (5)$$

while formula for the normal incidence is considered in this study due to low THz-beam aperture

$$r_{\text{m-k}} = \frac{\tilde{n}_m - \tilde{n}_k}{\tilde{n}_m + \tilde{n}_k}, \quad (6)$$

where \tilde{n}_m and \tilde{n}_k denote refractive indices of the media m , k .

2.3. THz solid immersion microscopy

Next, glioma model 101.8 was studied using novel THz imaging modality – the continuous-wave reflection-mode THz solid immersion microscopy adapted for imaging of soft biological tissues [40–42]. In-house THz microscope uses a backward-wave oscillator [43], as a THz-wave emitter at $\nu = 0.6$ THz (or $\lambda \approx 500 \mu\text{m}$), and a Golay cell [44], as a detector of the THz field intensity. It provides the spatial resolution up to 0.15λ [40], which is far beyond the Abbe diffraction limit of free-space focusing and might somewhat vary with optical properties of an imaged object [42]. The depth of field is around $0.1\text{--}0.2\lambda$ [41].

As shown in Fig. 3, THz solid immersion lens is a key element of our microscope, which is comprised of three components [40–42]:

- a rigidly-fixed wide-aperture aspherical HDPE singlet [45];
- a rigidly-fixed hypohemispherical lens, which is made of the High-Resistance Float-Zone silicon (HRFZ-Si), mounted in front of the focal plane in such a way that its spherical surface is almost concentric with the converging front of the THz wave and its flat surface is perpendicular to the optical axis;
- movable HRFZ-Si window, which is in contact with the flat surface of the HRFZ-Si hypohemisphere and is mounted on a motorized 2D translation stage.

The HRFZ-Si hypohemisphere and the HRFZ-Si window form a unitary optical element – the HRFZ-Si hemisphere that enhances the resolution of basic wide-aperture HDPE aspherical singlet by a factor of the HRFZ-Si refractive index at THz frequencies $n_{\text{Si}} \approx 3.415$ [40–42].

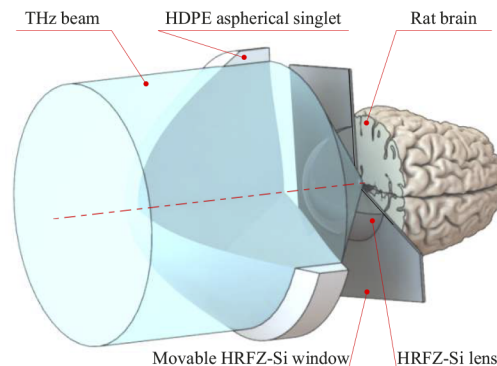


Fig. 3. Schematic of the rat brain imaging *ex vivo* using the original THz solid immersion microscope detailed in Refs. [40–42].

During the THz measurements, tissues *ex vivo* are handled at the shadow side of the HRFZ-Si window; see Fig. 3. They are raster-scanned by a focused THz beam thanks to the linear translations of the HRFZ-Si window in lateral directions [40]. The scanning step of $<0.075\lambda$ is used in order to satisfy the Whittaker–Nyquist–Kotelnikov–Shannon sampling theorem [46]. As a result of the measurements, a spatial distribution of the back-scattered THz field intensity is recorded $I(\mathbf{r})$, where \mathbf{r} is a radius-vector at the object plane. After digital processing of such images, spatial distribution of the THz refractive index over the imaged object surface $n(\mathbf{r})$ is inferred.

Since information only about the back-scattered THz-wave intensity $I(\mathbf{r})$ is detected in our THz microscope, while no data about phase is available, simultaneous reconstruction of the refractive index $n(\mathbf{r})$ and absorption coefficient $\alpha(\mathbf{r})$ of an imaged object appears to be an unsolved (or, at least, daunting) task. Obviously, in our future studies, we are going to mitigate this challenge by

using a THz-field detector, that yields both amplitude and phase information. But for now, we somewhat neglected the sample absorption α and resorted to estimation of only the real refractive index distributions $n(\mathbf{r})$ for the considered biological tissues.

By processing the THz microscopic images, real refractive index n at a given position \mathbf{r} of an imaged object surface is estimated via minimization of the error functional

$$n = \operatorname{argmin}_n \left[\frac{I_{\text{exp}}^{\text{obj}}}{I_{\text{exp}}^{\text{ref}}} - \frac{I_{\text{th}}(n)}{I_{\text{th}}(n_{\text{ref}})} \right] \quad (7)$$

where $I_{\text{exp}}^{\text{obj}}$ and $I_{\text{exp}}^{\text{ref}}$ stand for the object and reference intensities, that correspond to the THz-wave reflection from an object and a reference medium with an *a priori*-known refractive index n_{ref} . In this work, a free space behind the HRFZ-Si lens was used as a reference medium – $n_{\text{ref}} = 1.0$. The function $I_{\text{th}}(n)$ is a theoretical model, describing intensity of the back-scattered THz field for different refractive indices n of an object.

The theoretical model $I_{\text{th}}(n)$ is defined as follows

$$I_{\text{th}}(n) = \frac{1}{2} |E^{\text{s}}(n)|^2 + \frac{1}{2} |E^{\text{p}}(n)|^2, \quad (8)$$

where the first and second terms correspond to the amplitudes of orthogonal (s and p) polarization states, that exist within a wide THz beam aperture and are added incoherently. These amplitudes are comprised of the interfering ordinary-reflected waves and those from the Total Internal Reflection (TIR), that exist below ($\theta < \theta_{\text{TIR}}(n) = \arcsin(n/n_{\text{Si}})$) and above ($\theta \geq \theta_{\text{TIR}}(n)$) the critical angle of TIR effect, respectively. For s and p polarizations, the total amplitude of reflected wave can be calculated by integration of the solid immersion lens reflectivity $R^{\text{s/p}}(\theta, n)$ over the aperture angle θ

$$E^{\text{s/p}}(n) = E_0 \frac{\int_0^{\theta_{\text{max}}} R^{\text{s/p}}(\theta, n) \sin(\theta) d\theta}{\int_0^{\theta_{\text{max}}} \sin(\theta) d\theta}. \quad (9)$$

Here, E_0 is an amplitude of wave that radiates the Si hemisphere, and $\theta_{\text{max}} \approx 40^\circ$ is the maximal aperture angle of our solid immersion lens. The function $R^{\text{s/p}}(\theta, n)$ differs for the s and p polarizations and automatically accounts for the ordinary reflection ($\theta < \theta_{\text{TIR}}(n)$) or TIR ($\theta \geq \theta_{\text{TIR}}(n)$) conditions at the “Si-object” interface for the particular pair of n, θ . It also accounts for the multiple THz-wave reflections (standing waves) inside the HRFZ-Si hemispherical lens. In Eq. (9), the multiplication term $\sin(\theta)$ regulates a contribution of different aperture parts (with their elementary solid angle) to the resultant reflected wave. Evidently, such a contribution increases with θ with an increasing solid angle

$$\Omega = \iint_s \sin(\theta) d\phi d\theta, \quad (10)$$

where θ is the colatitude (angle from the optical axis) and ϕ is the longitude.

For the infinite coherence length of our backward-wave oscillator, $R^{\text{s/p}}$ is defined as follows

$$R^{\text{s/p}}(\theta, n) = r_{0\text{-Si}} + \frac{t_{0\text{-Si}} t_{\text{Si-0}} p_{\text{Si}}^2 r^{\text{s/p}}(\theta, n)}{1 - p_{\text{Si}}^2 r_{\text{Si-0}} r^{\text{s/p}}(\theta, n)}, \quad (11)$$

where $r_{0\text{-Si}}$, $r_{\text{Si-0}}$ and $t_{0\text{-Si}}$, $t_{\text{Si-0}}$ are the polarization-dependent Fresnel reflection and transmission coefficients (by field) at the normal incidence [31,47,48], corresponding to the “free space–Si”

and “Si–free space” interfaces; while p_{Si} is a THz-wave phase delay in the HRFZ-Si hemisphere governed by the modified Bouguer–Lambert–Beer law [31,47,48]

$$p_{\text{Si}} = \exp\left(-i\frac{2\pi\nu}{c_0}n_{\text{Si}}(l_1 + l_2)\right). \quad (12)$$

Parameter $r^{s/p}$ describes the object- and polarization-dependent Fresnel reflection (by field) at the “Si – object” interface, for the s and p polarization states. It is defined by the Fresnel formulas relying on the wave vector formalism:

$$\begin{aligned} r_{\text{Si/obj}}^s(n, \theta) &= \frac{k_{z,\text{Si}}(\theta) - k_{z,\text{obj}}(n, \theta)}{k_{z,\text{Si}}(\theta) + k_{z,\text{obj}}(n, \theta)}, \\ r_{\text{Si/obj}}^p(n, \theta) &= \frac{n^2 k_{z,\text{Si}}(\theta) - n_{\text{Si}}^2 k_{z,\text{obj}}(n, \theta)}{n^2 k_{z,\text{Si}}(\theta) + n_{\text{Si}}^2 k_{z,\text{obj}}(n, \theta)}, \end{aligned} \quad (13)$$

that govern both the ordinary-reflected ($\theta < \theta_{\text{TIR}}$) and TIR ($\theta \geq \theta_{\text{TIR}}$) waves, where

$$\begin{aligned} k_{z,\text{Si}}(\theta) &= \frac{2\pi\nu}{c_0}n_{\text{Si}}\cos(\theta), \\ k_{z,\text{obj}}(n, \theta) &= \frac{2\pi\nu}{c_0}\sqrt{n^2 - n_{\text{Si}}^2\sin^2(\theta)}. \end{aligned} \quad (14)$$

In Fig. 4, the resultant normalized reflectivity of our THz solid immersion lens is shown, as a function of refractive index n of an object handled at its shadow side. The inverse problem of the THz solid immersion microscopy can be solved unambiguously, when the object refractive index n is at the monotonic part of thus described reflectivity model. From Fig. 4, one can notice that typical refractive indices of tissues satisfy this requirement.

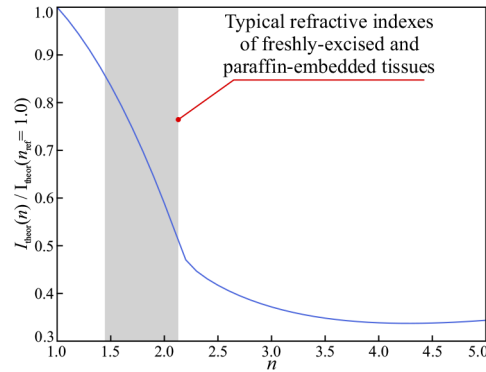


Fig. 4. Model of the normalized THz-wave reflectivity from the HRFZ-Si hemisphere, defined by Eqs. (7)–(14). Monotonic part of the theoretical curve ($n \leq 4.1$) can be used for estimation of the object refractive index n . Gray area shows typical range of the THz refractive indices of the freshly-excised and paraffin-embedded tissues.

Thus described method of inverse problem solution of the solid immersion microscopy yields estimation of the refractive index distribution over the object plane $n(\mathbf{r})$ at the free-space wavelength of $\lambda = 500 \mu\text{m}$ ($\nu \simeq 0.6 \text{ THz}$) based on the THz microscopic images $I(\mathbf{r})$, while a contribution of the object absorption coefficient α to the THz-wave reflection from the “Si–tissue” interface is somewhat neglected. This method is novel, and it deserved a separate comprehensive paper with all underlying aspects, assumptions, and computational routine, as well as with studies

of its stability in presence of such negative factors, as finite absorption coefficient α and thickness of a sample, its raw surface and spatial heterogeneity, as well as possible air gaps between the HRFZ-Si lens and a sample. We will consider these problems in a separate research paper. Meanwhile, in this paper, this method is already applied to process THz microscopic images of the rat brain tissues, aimed at quite a robust estimation of their refractive index distributions $n(\mathbf{r})$. Below, we show that the observed results mostly agree with our THz pulsed spectroscopy data, as well as with previous studies.

3. Results

In Fig. 5(a), (b), refractive index n and absorption coefficient α (by field), that are measured by the THz pulsed spectrometer with a diffraction limited resolution (see Sec. 2.2 and Eq. (1)), are shown for the intact rat brain and glioma model 101.8 *ex vivo*. The THz data were verified by the H&E-stained histology, as illustrated in Fig. 5(c). By measuring brain tissues with a focused THz beam in different positions over the whole rat brain (see Fig. 5(c)), fluctuations of the tissue response at THz frequencies were evaluated. Mean THz optical properties and their dispersion over the rat brain are shown by markers and error bars in Fig. 5, where the error bars define 95% confidential interval of measurements. Due to limitations in spatial resolution, we did not differentiate the intact tissue into white and grey matter, and we were unable to identify any subwavelength neurovascular structures and heterogeneities of the brain. In this way, THz pulsed spectroscopy study mostly aimed at evaluating the potential of this method for rough discrimination between the intact tissues and a tumor.

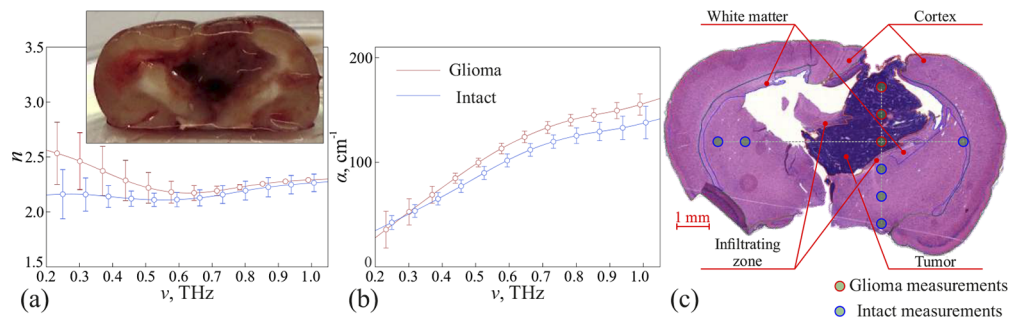


Fig. 5. THz optical properties of the freshly-excised intact rat brain tissues and glioma model 101.8 *ex vivo*. (a) Refractive index n . (b) Absorption coefficient α (by field). (c) Example of the H&E-stained histology, where blue- and red-colored markers indicate areas of intact tissues and glioma, that were studied by the THz pulsed spectroscopy. Insert in (a) shows a photo of the freshly-excised rat brain *ex vivo* after the scalpel incision through the tumor center.

As a result, THz pulsed spectroscopy of homograft glioma model 101.8 indeed confirmed a statistically-significant difference between THz response of the intact tissues and gliomas. Particularly, a tumor features the overall higher n and α in the THz range. At the same time, the observed difference is less pronounced than that reported in studies of the xenograft animal glioma models [25–30] and the WHO Grade I–IV human brain gliomas [31,35]. We also notice considerable dispersion of the THz optical properties across the sample, which was also reported in Refs. [25,31]. Such heterogeneity is assumed to originate from various neurovascular structures, fluctuations of the water content and cell density over the brain. However, the diffraction-limited resolution of common THz pulsed spectroscopy systems fails to ascertain the nature of such sub-wavelength structures and, thus, is incapable of confirming this hypothesis.

From Fig. 5, we also notice some fluctuations of thus measured optical properties, that are somewhat similar to those observed in earlier studies and that are not typical to the THz response

of tissues. Such modulations were previously observed in a number of Refs. [28,39], and they can originate due to few common negative factors inherent to the THz measurements of tissues [49–52], such as a limited performance of the applied THz pulsed spectrometer, problems in tissue positioning, tissue shrinkage and occlusions, variations of the tissue response over its aperture.

In Fig. 6, results of the THz solid immersion microscopy of the intact rat brain and glioma model 101.8 are shown, where both the freshly-excised and paraffin-embedded (dehydrated) tissues are considered. Panel (a) shows visible photos of the freshly-excised tissues, while panels (b),(c) show the measured THz images $I(\mathbf{r})$ and the inferred tissue refractive indexes $n(\mathbf{r})$, respectively. Panels (d)–(f) show the listed data set for the paraffin-embedded tissues, while panel (g) shows results of the H&E-stained histology. Histology yields qualitative verification of the THz imaging data; but one should take into account possible brain shift and shrinkage during resection, measurements, paraffin embedding, etc. Majority of thus collected THz images possesses quite high resolution, good contrast and low noise level, except for the image of paraffin-embedded glioma # 3 from Figs. 6(e),(f). The reason for distortions in these images is due to small curvature of an imaged paraffin block with embedded tissues, that leads to formation of air gaps between the HRFZ-Si window and a block and, thus, distorts the imaging data and makes its analysis problematic. Therefore, one should take special care of ensuring that the freshly-excised or paraffin-embedded tissues are in contact with the high-refractive index lens of the THz solid immersion microscope.

From Fig. 6, many mesoscale heterogeneities of both the intact rat brain and a tumor are evident. For example, markers I and II point to the visually distinct white and gray matters of the freshly-excised intact rat brain. The estimated refractive index, at 0.6 THz, of the intact tissues overall agrees well with the prior studies of healthy brain in the THz range; for example, see Refs. [28,30,31]. White matter features slightly higher refractive index than the gray one, which might be due to increased content of tissue water (in the form of an electrolyte solution inside the nerve cell axons) and myelin (a lipid-rich substance surrounding the nerve cell axons) [53]. Additionally, markers III, IV, V, and VI indicate other types of structural inhomogeneities, such as regions of tumor cells accumulation, tumor vessels, necrosis zone, and hemorrhage zone, correspondingly. A tumor possesses overall higher refractive index than the surrounding intact brain tissues, which agrees with the THz pulsed spectroscopy data from Fig. 5. However, a tumor can be somehow confused with higher-refractive-index white matter and edematous tissues. Similarity between the THz response of edematous tissues and a brain tumor was reported in few prior Refs. [31,33,35], while an ability to confuse between a tumor and a white matter is observed in this study for the first time. It is worth noting that differentiation between intact tissues and a tumor based on THz data from Fig. 6 appeared to be a daunting task due to the observed brain tissue heterogeneity. Indeed, much clearer tumor margins (including an ability for the univocal differentiation between white matter and a tumor) were observed in the THz images of xenograft glioma model from animals in Refs. [25,27–30], as compared to the considered homograft glioma 101.8. This highlights an importance of appropriate selection of glioma models for studying capabilities of novel brain tumor imaging modalities.

Moreover, by comparing THz images of the freshly-excised (hydrated) and paraffin-embedded (dehydrated) rat brains, we notice that a contrast between a tumor and intact tissues, as well as between different neurovascular structures of the brain, almost disappears in THz images of dehydrated tissues. Such effect was also observed in Ref. [25], which confirms that water is the main endogenous label of a tumor in the THz range. Some residual contrast in the THz images of the dehydrated brain tissues is probably due to other biochemical characteristics and variable cell density. Finally, it is well known that intramolecular vibrations of many biological compounds lay in the THz range, including proteins, lipids, amino acids, deoxyribonucleic acids,

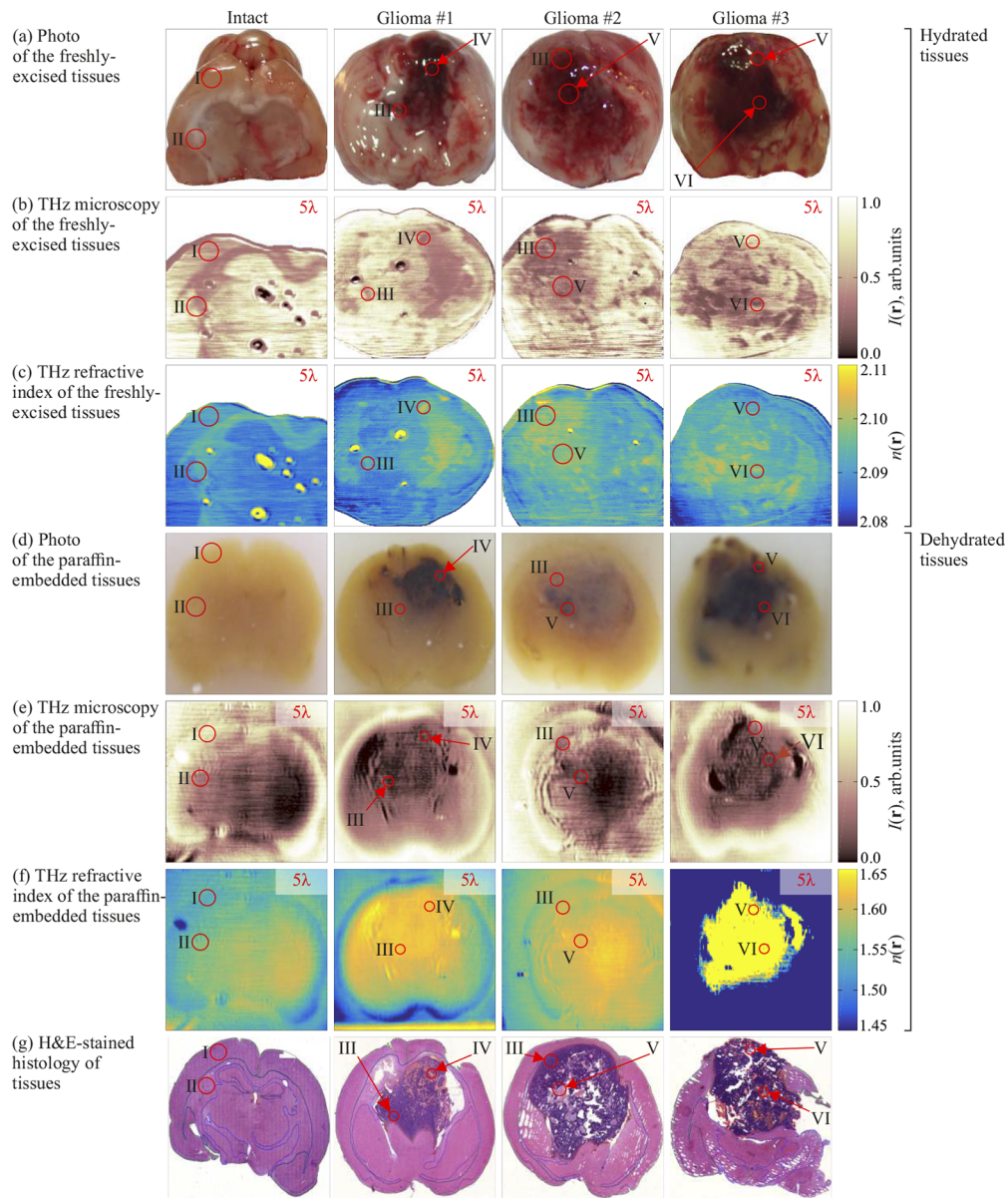


Fig. 6. THz solid immersion microscopy *ex vivo* at $\nu = 0.6$ THz ($\lambda \approx 500 \mu\text{m}$) of intact rat brain and glioma model 101.8. (a)–(c) Visible photos, THz images $I(\mathbf{r})$, and refractive index distributions $n(\mathbf{r})$ for the one freshly-excised intact brain and three tumor samples. (d)–(f) Equal data set for the paraffin-embedded tissues. (g) H&E-stained histology. Red circles with numbers denote the corresponding tissue fragments for various research methods. Particularly, I, II stand for the cerebral cortex and white matter, whereas III, IV, V, and VI stand for the accumulation of tumor cells, tumor vessels, necrosis zone, and hemorrhage zone, respectively.

etc. [54,55]. Along with water, these classes of biomolecules might contribute to the differences between tissues in the THz range.

4. Discussions

The described THz measurements *ex vivo* of the rat glioma model 101.8 lead to several important observations, that pose new challenging questions for the THz optics and biophotonics. By imaging of the brain tissues with a high-resolution THz solid immersion microscope, the tissue heterogeneity at the THz-wavelength scale was discovered for the first time. The observed structural inhomogeneities of both the intact tissues and a tumor lead to the mesoscale spatial fluctuation of their THz optical properties. In turn, these fluctuations should give rise to the Mie scattering of the THz waves in tissues.

Thus, a question arises about applicability of the standard effective medium theory and the related models of effective complex dielectric permittivity in the THz range [2,6,35]. Indeed, the effective medium theory assumes tissues to be homogeneous at the THz-wavelength scale and, thus, fails to take into account any non-Rayleigh scattering effects. It is worth noting that, in addition to the rat brain tissues, significant heterogeneity was previously observed in the breast and muscle tissues using the same THz microscope [40,41]. Therefore, the question of choosing a correct physical model for the THz data interpretation is important not only for the THz neurophotonics, but more generally for the THz biophotonics. This should push further research into realms of adapting the Mie scattering and radiation transfer theories for describing interactions between THz waves and tissues [56,57]. However, a problem of understanding the THz-wave scattering in tissues and the interplay between absorption and scattering phenomena is still to be unaddressed.

While certain differences between the effective THz response of the intact tissues and gliomas are measurable (see Refs. [25–31,35] and Fig. 5 of this work), heterogeneous character of tissues might strongly complicate the intraoperative THz delineation of tumor margins, making it a daunting (or even impossible) task; see Fig. 6. Common effective medium theory formalisms, that involve estimation of the effective optical properties of tissues averaged within the diffraction-limited THz beam spot, would probably not provide reliable enough data for the intraoperative delineation of the tumor margins. In order to make the THz neurodiagnosis possible, one should embrace novel modalities of THz spectroscopy and imaging [1,40–42], that overcome the Abbe diffraction limit and improve the tissue characterization. A comprehensive analysis of the brain tissue response at THz frequencies (with an emphasis on the perifocal region of a tumor) is in order to better understand the origin of these effects, as well as to introduce advanced approaches for the better tissue differentiation, that go far beyond a simple comparison of the effective THz dielectric response of tissues. At the same time, being comprehensively analyzed and modeled, heterogeneities of brain tissues can serve a source of additional useful information for the intraoperative THz discrimination of tissues.

The potential for the development of THz microscopy tools for detecting individual cell populations within the glioblastoma tissue seems to be an extremely important task that allows solving a number of fundamental and clinical problems. Internal heterogeneity of glioblastomas is a reflection of the key mechanisms of their pathogenesis; assessment of the properties of cell-population heterogeneity opens up broad prospects for the most accurate determination of the degree of neoplasm biological aggressiveness and potentially the most effective ways of treating it [58,59]. In particular, it is important to identify such a population of tumor cells as glioma stem cells, which are able to spread widely in the brain beyond the main tumor node [60,61]. At the same time, glioma stem cells are one of the main sources of tumor cell mass repopulation and, as a consequence, a key etiologic cause of recurrence [60,61]. Moreover, a variety of this type of cells in the form of a mesenchymal variant provides the formation of tumor resistance

to the applied approaches of chemotherapy and radiation therapy [62,63]. In this regard, the detection and resection of brain tissue infiltrated with these cell types seems to be a critical task for increasing the radicality of surgical treatment and a significant increase in the patients overall and disease-free survival rates. At the same time, the means of detecting such features of the tumor cell-population composition are very limited and rely mainly on single-cell sequencing approaches, which are extremely expensive and inapplicable in the conditions of intraoperative diagnostics [64,65]. Therefore, the development of new tools for intraoperative cell-population mapping of brain tissue, in particular THz microscopy, is an extremely important fundamental and clinical scientific task. Although THz solid immersion microscopy does not provide such a high spatial resolution, another THz imaging modalities such as THz scanning-probe near-field microscopy can provide resolution up to $\sim 10^{-3}$ – 10^{-4} [66,67] and allow to visualize cellular structures of tissues [68]. However, sensitivity of THz imaging and spectroscopic techniques to individual tumor cells and their populations is still a question requiring further investigations. We should notice that, in our work, we for the first time demonstrated tumor heterogeneity at the scales of THz wavelength, which gives the way to further solving of this problem.

We should notice again that number of noninvasive, minimally invasive and intraoperative approaches are being developed for glioma margins detection, such as MRI, fluorescence imaging, optical coherence tomography and Raman spectroscopy. However, they suffer from low spatial resolution, or far from clinical applications and do not provide enough efficiency for detecting different grades of brain glioma. THz imaging and spectroscopy can be considered as perspective tools for intraoperative neurodiagnosis, which have approved its efficiency for all grades (I–IV) of brain glioma and reveal endogenous contrast between tumors and intact tissues. At the same time, considerable research and engineering efforts are still required in order to objectively uncover capabilities of THz technology in the intraoperative neurodiagnosis of brain tumors, as well as to develop the related modalities of intraoperative spectroscopy and imaging of brain tissues in the THz range.

More generally, sub-wavelength-resolution THz imaging holds strong potential in different branches of neuroscience and neurodiagnosis. Overall, the question of molecular (particularly, protein and lipid) identity of different parts of the brain is extremely complex. For example, in the brains of mice and rats, in addition to significant differences in protein and lipid composition between gray and white matters, as detected by the THz microscopy, there are also significant regional differences in the areas of cortex [69,70]. As a highly specialized tissue, the brain contains finely tuned and functionally well-differentiated neurons and glial cells, the molecular basis of which underlies the difference in proteolipidemic profile. To some extent, THz microscopy is capable of visualizing the molecular heterogeneity of the brain tissue inherent to different regions of gray and white matters. However, in the THz images, subtle regional features are not as clearly defined.

Finally, for the brain tumors, the contrast in THz images, can generally be explained by significant differences in the molecular profile of glial neoplasms, especially glioblastomas, and intact glial tissue. Such changes are related to a wide range of proteins and lipids; while it is worth noting that modifications of proteome components occur as a result of mutations [71]. Moreover, THz microscopy allows us to consider the issues of intratumoral heterogeneity, which attracts increasing attention in the modern tumor research. First, it yields imaging of both histological heterogeneity of a tumor, which reflects such histological elements, as vessels and necrosis, that are fundamentally important in diagnostics. Second, it might be useful in studies of the cellular-population heterogeneity, that deals with different populations of tumor cells in gliomas with different molecular properties, including the proteomic and lipidomic features [58,72].

5. Conclusions

In this paper, rat glioma model 101.8 was studied *ex vivo* using the THz pulsed spectroscopy and the THz solid immersion microscopy with sub-wavelength spatial resolution. THz pulsed spectroscopy revealed differences between the effective optical properties of the intact tissues and a tumor, along with fluctuations of these properties over the rat brain. The THz microscopy showed heterogeneity of both the intact and pathologically-altered brain tissues at the THz-wavelength scale. Heterogeneity of the intact brain was attributed to distinct response of the white and gray matters, and of other neurovascular structures of the brain. In the case of a tumor, variation in the THz response comes from the necrotic debris and hemorrhage. Such heterogeneities might significantly complicate delineation of the tumor margins during an intraoperative THz neurodiagnosis. Our findings pose important problems of studying the heterogeneous character of brain tissues and the related THz-wave scattering effects. They revealed the need for applying the Mie scattering theory and the radiation transfer theory to describe the THz-wave – tissue interactions in different branches of THz biophotonics.

Funding. Russian Foundation for Basic Research (18-29-02060); Russian Science Foundation (17-79-20346).

Acknowledgements. Development of the experimental setups for THz spectroscopy and microscopy of tissues (by K.I. Zaytsev), as well as THz data processing (by A.A. Gavdush and P.V. Nikitin) was supported by the Russian Science Foundation, Project # 17-79-20346. The work with rat brain tissues, including its resection, preparation, histology, and analysis of the tissue heterogeneity (by N.V. Chernomyrdin and V.V. Tuchin) was supported by the Russian Foundation for Basic Research, Project # 18-29-02060.

Disclosures. The authors declare no conflict of interest.

Data availability. Data underlying the results presented in this paper are not publicly available at this time but may be obtained from the authors upon reasonable request.

References

1. H. Guerboukha, K. Nallappan, and M. Skorobogatiy, "Toward real-time terahertz imaging," *Adv. Opt. Photonics* **10**(4), 843–938 (2018).
2. K. Zaytsev, I. Dolganova, N. Chernomyrdin, G. Katyba, A. Gavdush, O. Cherkasova, G. Komandin, M. Shchedrina, A. Khodan, D. Ponomarev, I. Reshetov, V. Karasik, M. Skorobogatiy, V. Kurlov, and V. Tuchin, "The progress and perspectives of terahertz technology for diagnosis of neoplasms: a review," *J. Opt.* **22**(1), 013001 (2020).
3. P. Ashworth, E. Pickwell-MacPherson, E. Provenzano, S. Pinder, A. Purushotham, M. Pepper, and V. Wallace, "Terahertz pulsed spectroscopy of freshly excised human breast cancer," *Opt. Express* **17**(15), 12444–12454 (2009).
4. B. Truong, A. Fitzgerald, S. Fan, and V. Wallace, "Concentration analysis of breast tissue phantoms with terahertz spectroscopy," *Biomed. Opt. Express* **9**(3), 1334–1349 (2018).
5. M. Konnikova, O. Cherkasova, M. Nazarov, D. Vrazhnov, Y. Kistenev, S. Titov, E. Kopeikina, S. Shevchenko, and A. Shkurinov, "Malignant and benign thyroid nodule differentiation through the analysis of blood plasma with terahertz spectroscopy," *Biomed. Opt. Express* **12**(2), 1020–1035 (2021).
6. O. Smolyanskaya, N. Chernomyrdin, A. Konovko, K. Zaytsev, I. Ozheredov, O. Cherkasova, M. Nazarov, J.-P. Guillet, S. Kozlov, Y. Kistenev, J.-L. Coutaz, P. Mounaix, V. Vaks, J.-H. Son, H. Cheon, V. Wallace, Y. Feldman, I. Popov, A. Yaroslavsky, A. Shkurinov, and V. Tuchin, "Terahertz biophotonics as a tool for studies of dielectric and spectral properties of biological tissues and liquids," *Prog. Quantum Electron.* **62**, 1–77 (2018).
7. P. Wesseling and D. Capper, "WHO 2016 classification of gliomas," *Neuropathol. Appl. Neurobiol.* **44**(2), 139–150 (2018).
8. G. Musina, P. Nikitin, N. Chernomyrdin, I. Dolganova, A. Gavdush, G. Komandin, D. Ponomarev, A. Potapov, I. Reshetov, V. Tuchin, and K. Zaytsev, "Prospects of terahertz technology in diagnosis of human brain tumors – a review," *J. Biomed. Photonics Eng.* **6**(2), 020201 (2020).
9. Q. T. Ostrom, G. Cioffi, H. Gittleman, N. Patil, K. Waite, C. Kruchko, and J. S. Barnholtz-Sloan, "CBTRUS statistical report: primary brain and other central nervous system tumors diagnosed in the United States in 2012–2016," *Neuro-Oncology* **21**(Supplement_5), v1–v100 (2019).
10. T. J. Brown, M. C. Brennan, M. Li, E. W. Church, N. J. Brandmeir, K. L. Rakszawski, A. S. Patel, E. B. Rizk, D. Suki, R. Sawaya, and M. Glantz, "Association of the extent of resection with survival in glioblastoma: a systematic review and meta-analysis," *JAMA Oncol.* **2**(11), 1460–1469 (2016).
11. A. Jakola, A. Skjulsvik, K. Myrmel, K. Sjøvik, G. Unsgård, S. Torp, K. Aaberg, T. Berg, H. Dai, K. Johnsen, R. Kloster, and O. Solheim, "Surgical resection versus watchful waiting in low-grade gliomas," *Annals Oncol.* **28**(8), 1942–1948 (2017). Changes in serum IL-8 levels reflect and predict response to anti-PD-1 treatment in melanoma and NSCLC.

12. D. N. Louis, A. Perry, G. Reifenberger, A. von Deimling, D. Figarella-Branger, W. K. Cavenee, H. Ohgaki, O. D. Wiestler, P. Kleihues, and D. W. Ellison, "The 2016 world health organization classification of tumors of the central nervous system: a summary," *Acta Neuropathol.* **131**(6), 803–820 (2016).
13. I.-A. Rasmussen, F. Lindseth, O. Rygh, E. Berntsen, T. Selbekk, J. Xu, T. Hernes, E. Harg, A. Håberg, and G. Unsgård, "Functional neuronavigation combined with intra-operative 3D ultrasound: Initial experiences during surgical resections close to eloquent brain areas and future directions in automatic brain shift compensation of preoperative data," *The Lancet Oncol.* **149**(4), 365–378 (2007).
14. C. Senft, A. Bink, K. Franz, H. Vatter, T. Gasser, and V. Seifert, "Intraoperative mri guidance and extent of resection in glioma surgery: a randomised, controlled trial," *Lancet Oncol.* **12**(11), 997–1003 (2011).
15. N. Pustogarov, D. Pantelev, S. Goryaynov, A. Ryabova, E. Rybalkina, A. Revishchin, A. Potapov, and G. Pavlova, "Hiding in the shadows: CPOX expression and 5-ALA induced fluorescence in human glioma cells," *Mol. Neurobiol.* **54**(7), 5699–5708 (2017).
16. B. Chen, H. Wang, P. Ge, J. Zhao, W. Li, H. Gu, G. Wang, Y. Luo, and D. Chen, "Gross total resection of glioma with the intraoperative fluorescence-guidance of fluorescein sodium," *Int. J. Med. Sci.* **9**(8), 708–714 (2012).
17. S. A. Goryaynov, V. A. Okhlopkov, D. A. Golbin, K. A. Chernyshov, D. V. Svistov, B. V. Martynov, A. V. Kim, V. A. Byvaltsev, G. V. Pavlova, A. Batalov, N. A. Konovalov, P. V. Zelenkov, V. B. Loschenov, and A. A. Potapov, "Fluorescence diagnosis in neurooncology: retrospective analysis of 653 cases," *Front. Oncol.* **9**, 830 (2019).
18. E. B. Kiseleva, K. S. Yashin, A. A. Moiseev, L. B. Timofeeva, V. V. Kudelkina, A. I. Alekseeva, S. V. Meshkova, A. V. Polozova, G. V. Gelikonov, E. V. Zagaynova, and N. D. Gladkova, "Optical coefficients as tools for increasing the optical coherence tomography contrast for normal brain visualization and glioblastoma detection," *Neurophotonics* **6**(03), 1 (2019).
19. I. N. Dolganova, P. V. Aleksandrova, P. V. Nikitin, A. I. Alekseeva, N. V. Chernomyrdin, G. R. Musina, S. T. Beshplav, I. V. Reshetov, A. A. Potapov, V. N. Kurlov, V. V. Tuchin, and K. I. Zaytsev, "Capability of physically reasonable OCT-based differentiation between intact brain tissues, human brain gliomas of different WHO grades, and glioma model 101.8 from rats," *Biomed. Opt. Express* **11**(11), 6780–6798 (2020).
20. D. Orringer, B. Pandian, Y. Niknafs, T. Hollon, J. Boyle, S. Lewis, M. Garrard, S. Hervey-Jumper, H. Garton, C. Maher, J. Heth, O. Sagher, D. Wilkinson, M. Snuderl, S. Venneti, S. Ramkissoon, K. McFadden, A. Fisher-Hubbard, A. Lieberman, and S. Camelo-Piragua, "Rapid intraoperative histology of unprocessed surgical specimens via fibre-laser-based stimulated raman scattering microscopy," *Nat. Biomed. Eng.* **1**(2), 0027 (2017).
21. D. Wirth, T. Smith, R. Moser, and A. Yaroslavsky, "Demeclocycline as a contrast agent for detecting brain neoplasms using confocal microscopy," *Phys. Med. Biol.* **60**(7), 3003–3011 (2015).
22. X. Feng, A. Muzikansky, A. Ross, M. Hamblin, P. Jermain, and A. Yaroslavsky, "Multimodal quantitative imaging of brain cancer in cultured cells," *Biomed. Opt. Express* **10**(8), 4237–4248 (2019).
23. E. Genina, A. Bashkatov, D. Tuchina, P. Timoshina, N. Navolokin, A. Shirokov, A. Khorovodov, A. Terskov, M. Klimova, A. Mamedova, I. Blokhina, I. Agranovich, E. Zinchenko, O. Glushkovskaya, and V. Tuchin, "Optical properties of brain tissues at the different stages of glioma development in rats: pilot study," *Biomed. Opt. Express* **10**(10), 5182 (2019).
24. M. Kircher, A. de la Zerda, J. Jokerst, C. Zavaleta, P. Kempen, E. Mittra, K. Pitter, R. Huang, C. Campos, F. Habte, R. Sinclair, C. Brennan, I. Mellinghoff, E. Holland, and S. Gambhir, "A brain tumor molecular imaging strategy using a new triple-modality MRI-photoacoustic-Raman nanoparticle," *Nat. Med.* **18**(5), 829–834 (2012).
25. S. Oh, S.-H. Kim, Y. Ji, K. Jeong, Y. Park, J. Yang, D. Park, S. Noh, S.-G. Kang, Y.-M. Huh, J.-H. Son, and J.-S. Suh, "Study of freshly excised brain tissues using terahertz imaging," *Biomed. Opt. Express* **5**(8), 2837–2842 (2014).
26. K. Meng, T.-N. Chen, T. Chen, L.-G. Zhu, Q. Liu, Z. Li, F. Li, Z.-R. Zhong, S.-C. Li, H. Feng, and J.-H. Zhao, "Terahertz pulsed spectroscopy of paraffin-embedded brain glioma," *J. Biomed. Opt.* **19**(7), 077001 (2014).
27. S. Yamaguchi, Y. Fukushi, O. Kubota, T. Itsuji, T. Ouchi, and S. Yamamoto, "Origin and quantification of differences between normal and tumor tissues observed by terahertz spectroscopy," *Phys. Med. Biol.* **61**(18), 6808–6820 (2016).
28. S. Yamaguchi, Y. Fukushi, O. Kubota, T. Itsuji, T. Ouchi, and S. Yamamoto, "Brain tumor imaging of rat fresh tissue using terahertz spectroscopy," *Sci. Rep.* **6**(1), 30124 (2016).
29. Y. Ji, S. Oh, S. Kang, J. Heo, S. Kim, Y. Choi, S. Song, H. Son, S. Kim, J. Lee, S. Haam, Y. Huh, J. Chang, C. Joo, and J. Suh, "Terahertz reflectometry imaging for low and high grade gliomas," *Sci. Rep.* **6**(1), 36040 (2016).
30. L. Wu, D. Xu, Y. Wang, B. Liao, Z. Jiang, L. Zhao, Z. Sun, N. Wu, T. Chen, H. Feng, and J. Yao, "Study of *in vivo* brain glioma in a mouse model using continuous-wave terahertz reflection imaging," *Biomed. Opt. Express* **10**(8), 3953–3962 (2019).
31. A. Gavdush, N. Chernomyrdin, K. Malakhov, S.-I. Beshplav, I. Dolganova, A. Kosyrkova, P. Nikitin, G. Musina, G. Katyba, I. Reshetov, O. Cherkasova, G. Komandin, V. Karasik, A. Potapov, V. Tuchin, and K. Zaytsev, "Terahertz spectroscopy of gelatin-embedded human brain gliomas of different grades: a road toward intraoperative THZ diagnosis," *J. Biomed. Opt.* **24**(02), 1 (2019).
32. S. Fan, B. Ung, E. Parrott, and E. Pickwell-MacPherson, "Gelatin embedding: a novel way to preserve biological samples for terahertz imaging and spectroscopy," *Phys. Med. Biol.* **60**(7), 2703–2713 (2015).
33. H. Zhao, Y. Wang, L. Chen, J. Shi, K. Ma, L. Tang, D. Xu, J. Yao, H. Feng, and T. Chen, "High-sensitivity terahertz imaging of traumatic brain injury in a rat model," *J. Biomed. Opt.* **23**(4), 036015 (2018).
34. J. Shi, Y. Wang, T. Chen, D. Xu, H. Zhao, L. Chen, C. Yan, L. Tang, Y. He, H. Feng, and J. Yao, "Automatic evaluation of traumatic brain injury based on terahertz imaging with machine learning," *Opt. Express* **26**(5), 6371–6381 (2018).

35. A. Gavdush, N. Chernomyrdin, G. Komandin, I. Dolganova, P. Nikitin, G. Musina, G. Katyba, A. Kucheryavenko, I. Reshetov, A. Potapov, V. Tuchin, and K. Zaytsev, "Terahertz dielectric spectroscopy of human brain gliomas and intact tissues *ex vivo*: double-Debye and double-overdamped-oscillator models of dielectric response," *Biomed. Opt. Express* **12**(1), 69–83 (2021).
36. V. Fedoseeva, E. Postovalova, A. Khalansky, V. Razzhivina, S. Gelperina, and O. Makarova, "Drug-induced pathomorphosis of glioblastoma 101.8 in wistar rats treated with doxorubicin bound to poly(lactide-co-glycolide) nanoparticles," *Sovrem. Tehnol. Med.* **10**(4), 105–112 (2018).
37. S. C. Steiniger, J. Kreuter, A. S. Khalansky, I. N. Skidan, A. I. Bobruskin, Z. S. Smirnova, S. E. Severin, R. Uhl, M. Kock, K. D. Geiger, and S. E. Gelperina, "Chemotherapy of glioblastoma in rats using doxorubicin-loaded nanoparticles," *Int. J. Cancer* **109**(5), 759–767 (2004).
38. K. Zaytsev, K. Kudrin, V. Karasik, I. Reshetov, and S. Yurchenko, "*In vivo* terahertz spectroscopy of pigmented skin nevi: Pilot study of non-invasive early diagnosis of dysplasia," *Appl. Phys. Lett.* **106**(5), 053702 (2015).
39. K. Zaytsev, A. Gavdush, N. Chernomyrdin, and S. Yurchenko, "Highly accurate *in vivo* terahertz spectroscopy of healthy skin: Variation of refractive index and absorption coefficient along the human body," *IEEE Trans. Terahertz Sci. Technol.* **5**(5), 817–827 (2015).
40. N. Chernomyrdin, A. Kucheryavenko, G. Kolontaeva, G. Katyba, I. Dolganova, P. Karalkin, D. Ponomarev, V. Kurlov, I. Reshetov, M. Skorobogatiy, V. Tuchin, and K. Zaytsev, "Reflection-mode continuous-wave 0.15- λ -resolution terahertz solid immersion microscopy of soft biological tissues," *Appl. Phys. Lett.* **113**(11), 111102 (2018).
41. N. V. Chernomyrdin, V. A. Zhelnov, A. S. Kucheryavenko, I. N. Dolganova, G. M. Katyba, V. E. Karasik, I. V. Reshetov, and K. I. Zaytsev, "Numerical analysis and experimental study of terahertz solid immersion microscopy," *Opt. Eng.* **59**(06), 1 (2019).
42. V. Zhelnov, K. Zaytsev, A. Kucheryavenko, G. Katyba, I. Dolganova, D. Ponomarev, V. Kurlov, M. Skorobogatiy, and N. Chernomyrdin, "Object-dependent spatial resolution of the reflection-mode terahertz solid immersion microscopy," *Opt. Express* **29**(3), 3553–3566 (2021).
43. G. Komandin, S. Chuchupal, S. Lebedev, Y. Goncharov, A. Korolev, O. Porodinkov, I. Spektor, and A. Volkov, "BWO generators for terahertz dielectric measurements," *IEEE Trans. Terahertz Sci. Technol.* **3**(4), 440–444 (2013).
44. M. J. E. Golay, "Theoretical consideration in heat and infra-red detection, with particular reference to the pneumatic detector," *Rev. Sci. Instrum.* **18**(5), 347–356 (1947).
45. N. V. Chernomyrdin, M. E. Frolov, S. P. Lebedev, I. V. Reshetov, I. E. Spektor, V. L. Tolstoguzov, V. E. Karasik, A. M. Khorokhorov, K. I. Koshelev, A. O. Schadko, S. O. Yurchenko, and K. I. Zaytsev, "Wide-aperture aspherical lens for high-resolution terahertz imaging," *Rev. Sci. Instrum.* **88**(1), 014703 (2017).
46. C. Shannon, "Communication in the presence of noise," *Proc. IRE* **37**(1), 10–21 (1949).
47. K. Zaytsev, A. Gavdush, V. Karasik, V. Alekhnovich, P. Nosov, V. Lazarev, I. Reshetov, and S. Yurchenko, "Accuracy of sample material parameters reconstruction using terahertz pulsed spectroscopy," *J. Appl. Phys.* **115**(19), 193105 (2014).
48. B. Giuliano, A. Gavdush, B. Muller, K. Zaytsev, T. Grassi, A. Ivlev, M. Palumbo, G. Baratta, C. Scire, G. Komandin, S. Yurchenko, and P. Caselli, "Broadband spectroscopy of astrophysical ice analogues – I. Direct measurement of the complex refractive index of CO ice using terahertz time-domain spectroscopy," *A&A* **629**, A112 (2019).
49. Q. Sun, E. Parrott, Y. He, and E. Pickwell-MacPherson, "*In vivo* THz imaging of human skin: Accounting for occlusion effects," *J. Biophotonics* **11**(2), e201700111 (2018).
50. S. Fan, E. Parrott, B. Ung, and E. Pickwell-MacPherson, "Calibration method to improve the accuracy of THz imaging and spectroscopy in reflection geometry," *Photonics Res.* **4**(3), A29–A35 (2016).
51. X. Chen, Q. Sun, J. Wang, and E. Pickwell-MacPherson, "Skin surface feature influence on terahertz *in vivo* measurements," in *2020 45th International Conference on Infrared, Millimeter, and Terahertz Waves (IRMMW-THz)*, (2020), pp. 1–2.
52. H. Lindley-Hatcher, A. Hernandez-Serrano, Q. Sun, J. Wang, J. Cebrian, L. Blasco, and E. Pickwell-MacPherson, "A robust protocol for *in vivo* THz skin measurements," *J. Infrared, Millimeter, Terahertz Waves* **40**(9), 980–989 (2019).
53. Y. Zou, J. Li, Y. Cui, P. Tang, L. Du, T. Chen, K. Meng, Q. Liu, H. Feng, J. Zhao, M. Chen, and L.-G. Zhu, "Terahertz spectroscopic diagnosis of myelin deficit brain in mice and rhesus monkey with chemometric techniques," *Sci. Rep.* **7**(1), 5176 (2017).
54. K. Niessen, M. Xu, D. George, M. Chen, A. Ferre-D'Amare, E. Snell, V. Cody, J. Pace, M. Schmidt, and A. Markelz, "Protein and RNA dynamical fingerprinting," *Nat. Commun.* **10**(1), 1026 (2019).
55. H. Cheon, H.-J. Yang, S.-H. Lee, Y. Kim, and J.-H. Son, "Terahertz molecular resonance of cancer DNA," *Sci. Rep.* **6**(1), 37103 (2016).
56. V. Tuchin, *Tissue Optics: Light Scattering Methods and Instruments for Medical Diagnosis*, 3rd Edition (SPIE, 2015).
57. A. Ishimaru, *Electromagnetic Wave Propagation, Radiation, and Scattering: From Fundamentals to Applications*, 2nd Edition (IEEE Press, 2017).
58. C. Neftel, J. Laffy, M. G. Filbin, T. Hara, M. E. Shore, G. J. Rahme, A. R. Richman, D. Silverbush, M. L. Shaw, C. M. Hebert, J. Dewitt, S. Gritsch, E. M. Perez, L. N. Gonzalez Castro, X. Lan, N. Druck, C. Rodman, D. Dionne, A. Kaplan, M. S. Bertalan, J. Small, K. Pelton, S. Becker, D. Bonal, Q.-D. Nguyen, R. L. Servis, J. M. Fung, R. Mylvaganam, L. Mayr, J. Gojo, C. Haberler, R. Geyeregger, T. Czech, I. Slavic, B. V. Nahed, W. T. Curry, B. S. Carter, H. Wakimoto, P. K. Brastianos, T. T. Batchelor, A. Stemmer-Rachamimov, M. Martinez-Lage, M. P. Frosch, I. Stamenkovic, N. Riggi, E. Rheinbay, M. Monje, O. Rozenblatt-Rosen, D. P. Cahill, A. P. Patel, T. Hunter, I. M.

- Verma, K. L. Ligon, D. N. Louis, A. Regev, B. E. Bernstein, I. Tirosh, and M. L. Suvà, "An integrative model of cellular states, plasticity, and genetics for glioblastoma," *Cell* **178**(4), 835–849.e21 (2019).
59. A. Dirkse, A. Golebiewska, T. Buder, P. V. Nazarov, A. Muller, S. Poovathingal, N. H. C. Brons, S. Leite, N. Sauvageot, D. Sarkisjan, M. Seyfrid, S. Fritah, D. Stieber, A. Michelucci, F. Hertel, C. Herold-Mende, F. Azuaje, A. Skupin, R. Bjerkgvig, A. Deutsch, A. Voss-Böhme, and S. P. Niclou, "Stem cell-associated heterogeneity in Glioblastoma results from intrinsic tumor plasticity shaped by the microenvironment," *Nat. Commun.* **10**(1), 1787 (2019).
60. A. Sattiraju, K. K. S. Sai, and A. Mintz, "Glioblastoma Stem Cells and Their Microenvironment," *Stem Cell Microenviron. Beyond* **1041**, 119–140 (2017).
61. D. Zhou, B. M. Alver, S. Li, R. A. Hlady, J. J. Thompson, M. A. Schroeder, J.-H. Lee, J. Qiu, P. H. Schwartz, J. N. Sarkaria, and K. D. Robertson, "Distinctive epigenomes characterize glioma stem cells and their response to differentiation cues," *Genome Biol.* **19**(1), 43 (2018).
62. J. Behnan, G. Finocchiaro, and G. Hanna, "The landscape of the mesenchymal signature in brain tumours," *Brain* **142**(4), 847–866 (2019).
63. M. Fedele, L. Cerchia, S. Pegoraro, R. Sgarra, and G. Manfioletti, "Proneural-mesenchymal transition: phenotypic plasticity to acquire multitherapy resistance in glioblastoma," *Int. J. Mol. Sci.* **20**(11), 2746 (2019).
64. X. Ren, B. Kang, and Z. Zhang, "Understanding tumor ecosystems by single-cell sequencing: promises and limitations," *Genome Biol.* **19**(1), 211 (2018).
65. F. Wu, J. Fan, J. Fang, P. S. Dalvi, M. Odenthal, and N. Fang, "Single cell sequencing: a new dimension in cancer diagnosis and treatment," *Single-cell Sequen. Methylation* **1255**, 109–121 (2020).
66. H.-T. Chen, R. Kersting, and G. C. Cho, "Terahertz imaging with nanometer resolution," *Appl. Phys. Lett.* **83**(15), 3009–3011 (2003).
67. A. J. Huber, F. Keilmann, J. Wittborn, J. Aizpurua, and R. Hillenbrand, "Terahertz near-field nanoscopy of mobile carriers in single semiconductor nanodevices," *Nano Lett.* **8**(11), 3766–3770 (2008).
68. F. Formanek, M.-A. Brun, and A. Yasuda, "Contrast improvement of terahertz images of thin histopathologic sections," *Biomed. Opt. Express* **2**(1), 58 (2011).
69. R. Hodge, T. Bakken, J. Miller, K. Smith, E. Barkan, L. Graybuck, J. Close, B. Long, N. Johansen, O. Penn, Z. Yao, J. Eggermont, T. Höllt, B. Levi, S. Shehata, B. Aevermann, A. Beller, D. Bertagnolli, K. Brouner, and E. Lein, "Conserved cell types with divergent features in human versus mouse cortex," *Nature* **573**(7772), 61–68 (2019).
70. A. B. Rosenberg, C. M. Roco, R. A. Muscat, A. Kuchina, P. Sample, Z. Yao, L. T. Graybuck, D. J. Peeler, S. Mukherjee, W. Chen, S. H. Pun, D. L. Sellers, B. Tasic, and G. Seelig, "Single-cell profiling of the developing mouse brain and spinal cord with split-pool barcoding," *Science* **360**(6385), 176–182 (2018).
71. G. Reifenberger, H.-G. Wirsching, C. Knobbe-Thomsen, and M. Weller, "Advances in the molecular genetics of gliomas - implications for classification and therapy," *Nat. Rev. Clin. Oncol.* **14**(7), 434–452 (2017).
72. M. Papale, M. Buccarelli, C. Mollinari, M. A. Russo, R. Pallini, L. Ricci-Vitiani, and M. Tafani, "Hypoxia, inflammation and necrosis as determinants of glioblastoma cancer stem cells progression," *Int. J. Mol. Sci.* **21**(8), 2660 (2020).